Review of Scientific Instruments

RESEARCH ARTICLE | MAY 02 2024

Spot size measurement of a deuterium–tritium dense plasma focus using neutron radiography

L. Tafoya ; V. Geppert-Kleinrath ; J. Allison ; S. Baker; J. Bundgaard ; M. Freeman ; A. Hayes-Sterbenz ; G. Jungman; H. Li ; S. Li ; D. Lowe; J. Tybo; C. Wilde

Rev. Sci. Instrum. 95, 053501 (2024)
https://doi.org/10.1063/5.0187567

Review of Scientific Instruments ARTICLE pubs.aip.org/aip/rsi

Spot size measurement of a deuterium–tritium dense plasma focus using neutron radiography

Cite as: Rev. Sci. Instrum. 95, 053501 (2024); doi: 10.1063/5.0187567
Submitted: 14 November 2023 • Accepted: 5 April 2024 •
Published Online: 2 May 2024

L. Tafoya,[1,a)] V. Geppert-Kleinrath,[1] J. Allison,[1] S. Baker,[2] J. Bundgaard,[2] M. Freeman,[1] A. Hayes-Sterbenz,[1] G. Jungman,[1] H. Li,[1] S. Li,[1] D. Lowe,[2] J. Tybo,[1] and C. Wilde[1]

AFFILIATIONS

[1] Los Alamos National Laboratory, Los Alamos, New Mexico 87545, USA
[2] Nevada National Security Site, Las Vegas, Nevada 89030, USA

[a)] **Author to whom correspondence should be addressed:** ltafoya@lanl.gov

ABSTRACT

Neutron radiography is a technique uniquely suited to applications in nuclear diagnostics, non-destructive testing, and subcritical experiments. The spatial resolution of neutron radiographs is degraded by optical blur in the imaging system and the neutron source size, where the ideal source is point-like to optimize the point-spread function. A potential neutron source for radiography is the dense plasma focus (DPF), a coaxial Z-pinch that produces thermonuclear and beam-target neutrons. To assess if the source size is suitable for radiography, a neutron imaging system was used to measure the source size of the 4 MA Sodium DPF at the Nevada National Security Site operating with deuterium–tritium gas-fill. The source size was measured using the edge-spread function of tungsten objects, each having a rolled (convex) edge. The spot size was found to be 7–12 mm full-width at half-max (FWHM) assuming a Gaussian source, though comparison is presented for Lorentzian and Bennett distributions. The average FWHM was found to be 8.6 ± 1.2 mm vertically and 10.8 ± 1.2 mm horizontally with respect to the image plane, averaging over varied edges and alignments. The results were sensitive to source alignment and edge metrology, which introduced notable uncertainties. These results are consistent with separate experimental measurements as well as magnetohydrodynamics simulations of this DPF, which suggest that neutron production can originate from pinches ~5–7 mm off-axis. These results suggest that the DPF should be used for radiography at low magnification ($M < 1$) where spot size does not dominate spatial blur.

I. INTRODUCTION

Neutrons interact in material through collisions with constituent nuclei, as opposed to charged particles that also interact electromagnetically. As a result, neutrons more readily penetrate high-Z materials that are difficult to probe otherwise. Therefore, neutron radiography is uniquely suited to investigate systems where conventional techniques, such as x-ray and proton radiography,[1,2] might fail. A considerable limitation of employing this technique is the neutron source, in that radiography requires high yield for sufficient contrast but a small source (or spot) size for sufficient resolution. As such, source characterization of high yield neutron generators is a subject of ongoing interest.

One such neutron source is the dense plasma focus (DPF), a coaxial Z-pinch device that electromagnetically accelerates and compresses a plasma sheath.[3] The pinch region can reach sufficient energy-density for nuclear fusion of the ion species; hence, the DPF can operate as a neutron generator when the ionized gas is deuterium (DD-reactions, 2.45 MeV neutron emission) or a deuterium–tritium mix (DT-reactions, 14.1 MeV neutron emission). Several ongoing platforms are investigating the application of the DPF to neutron radiography.[4,5] A typical DPF configuration is shown in Fig. 1, which consists of a central anode rod surrounded by an outer ring of cathode rods. Flashover across the anode–cathode gap ionizes gas in the chamber (DD or DT), and radial current density $\mathbf{j}$ in the plasma produces an azimuthal magnetic field $\mathbf{B}$. The $\mathbf{j} \times \mathbf{B}$ force then pushes the plasma sheath toward the anode tip (referred to as the run-down phase), during which additional DT in the gap is swept up by the sheath. Once the current sheath expands further axially than the anode tip, azimuthal magnetic pressure compresses the plasma radially inward (the run-in phase). The system is now comparable to a Z-pinch such that the plasma implodes on-axis (the pinch phase).

Neutron production in the DPF is driven by thermonuclear and beam-target fusion of the ion species. While thermonuclear conditions are achieved from the on-axis implosion (a Z-pinch),

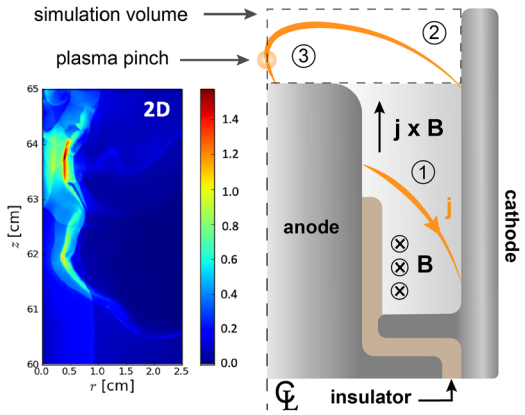

FIG. 1. (Right) Diagram of a DPF cross-section, cylindrically symmetric about the center-line (CL). Breakdown across the anode–cathode gap of the fill-gas produces a current-carrying plasma sheath that is accelerated axially by the $\mathbf{j} \times \mathbf{B}$ force (run-down phase, 1). Above the anode height, azimuthal magnetic field $\mathbf{B}$ radially compresses the sheath (run-in phase, 2) until the plasma implodes on-axis (pinch phase, 3). (Left) A 2D magnetohydrodynamic simulation of the plasma pinch at peak density (see Sec. VI).

beam-target neutrons are generated from instability-driven electric fields at the pinch that accelerate ions to high energies.[6] At the time of this experiment, the 4 MA Sodium DPF at the Nevada National Security Site (NNSS) was capable of producing total neutron yields in excess of 10^{12} per shot when run with DT, making it an appealing candidate for flash (pulsed) neutron radiography.[7]

Though the DPF is a robust neutron generator, its usability for radiography depends on the source size, as illustrated in Fig. 2. If the neutron production volume is large—that is, if the radiography source is distinctly not point-like—then the image will be blurred based on this size. The neutron source size can thus be determined from radiographs by measuring the blur.

The resolution (or blur) can be described using the point spread function (PSF), which determines how a point at the source plane is reproduced at the image plane. For point-projection radiography, it is then equivalent to the normalized source intensity distribution.[8] The PSF can be difficult to probe experimentally, even for a point-like neutron source, on account of neutron transmission through aperture edges. Instead, it is often more convenient to infer the PSF using either the edge spread function (ESF) or the line spread function (LSF), which are all related via a series of integrations. As the names suggest, the ESF describes the blurring of a perfect edge, while the LSF describes the blurring of a perfect line. The first derivative of the ESF is the LSF,

$$ESF(x) = \int_{-\infty}^{x} LSF(x')dx', \tag{1}$$

and the LSF describes a planar projection of the PSF,

$$LSF(x) = \int_{-\infty}^{\infty} PSF(x,y)dy. \tag{2}$$

Further derivation to obtain the PSF, modulation transfer function (MTF), and other radiographic quantities can be found in Refs. 8 and 9. Figure 2 also shows the ESF of a perfect edge from the point source vs the ESF of a blurred edge from the extended source.

Determination of the ESF requires a high-contrast edge, which in traditional imaging can typically be obtained using a knife edge object. However, the unique attenuation properties of neutrons would require a long, high-Z object and perfect alignment with the source to obtain the same result. Instead, a thick tungsten rolled edge (or rollbar[9]) is commonly employed in neutron imaging to add alignment flexibility.[10–12] Figure 3 illustrates how the ESF changes with source alignment for a knife-edge, whereas the change is minimal for a rolled edge.

From Fig. 2, it is also important to note that the source is magnified by a factor D_2/D_1 at the image plane, while the roll-height (sagitta) of a rolled edge placed at the aperture plane should be magnified by a factor $D_1/(D_1 + D_2)$ at the image plane.

Although Eq. (1) can be used to extract the LSF from a measured ESF, it can be difficult to numerically differentiate experimental ESF data depending on the signal-to-noise ratio. A moving average, filter, or down-sampling technique can be used to avoid noise amplification during differentiation,[14] but the acceptable degree of smoothing is often arbitrary. Without sufficiently high signal-to-noise, directly fitting the ESF to a physics-based transfer function is a more robust method. The fit ESF should be a convolution of the expected neutron transmission across the edge (roughly a step function, shown in Fig. 3) with the total blur caused by both the detector and the neutron source. Note that if both of

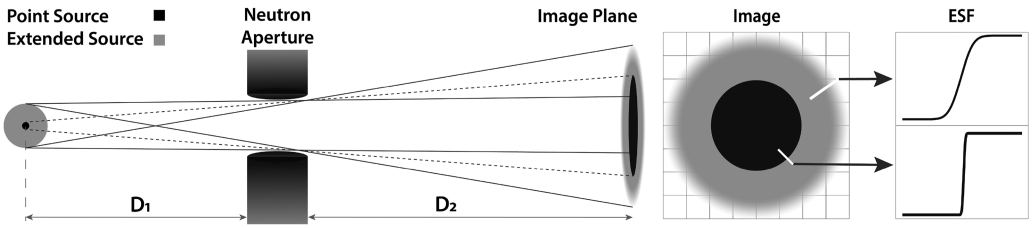

FIG. 2. Imaging through an aperture will produce blur based on the source size, as illustrated for a point source (black with dashed rays) vs a larger source (gray with solid rays). While the ideal edge-spread function (ESF) of a point-source would be a step-function (right bottom), a finite focal spot size will blur the step into a broadened transfer function (right top). The distances D_1 and D_2 also determine the source magnification, M, at the image plane: $M = D_2/D_1$.

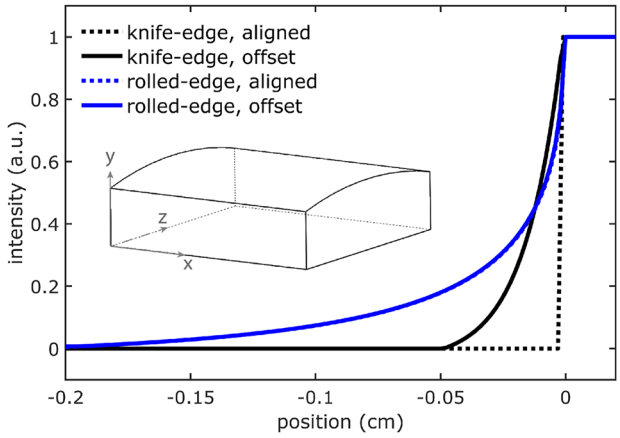

FIG. 3. Simulated edge spread functions (no blur) using MCNP6[13] for knife edge (flat) and rolled edge (rolled) tungsten blocks with the neutron source both aligned and offset. The wireframe cutout illustrates a rolled edge block and coordinate system for the setup. A point neutron source at $z = -0.20$ m was projected to a detector at $z = 12$ m to significantly magnify the tungsten edge. The aligned source was level in y with the peak of the edge roll, while the misaligned source was offset 2 cm in the $-y$ direction. Note that the aligned and offset rolled edge traces are identical, while the knife edge varies.

these blur components are assumed to be Gaussian distributed, they can be deconvolved from each other relatively simply via a sum of quadrature,

$$\sigma^2_{image} = \sigma^2_{source} + \sigma^2_{detector}. \tag{3}$$

This ESF fit technique has been used previously to characterize image blur in fast neutron radiography.[11] The $\sigma_{detector}$ contribution is specific to the optical components that comprise the imaging system. For scintillator-based neutron imaging, this term is generally dominated by the monolithic scintillator rather than the lens, mirror, or camera, given that the recoil-proton mechanism that drives the conversion of neutrons to visible light occurs throughout the scintillator volume.[15] Thicker scintillators increase the neutron conversion efficiency but also increase image blur as more light is produced outside the focal plane of the lens. Telecentric lenses can be employed to mitigate this effect.[10]

II. ANALYTICAL METHODS

The ESF fit function is constructed by convolving the expected edge transmission at the detector with a blur kernel described by the neutron source. The ideal edge response is a step function modified to include transmission through the rolled edge, which can be described analytically using the neutron mean free path in tungsten and the path length through the rolled edge (the chord). Transmission through the rolled edge $R(x)$ is then given by

$$R(x) = \exp\left(-\frac{2}{\lambda}\sqrt{2r\Delta x - (\Delta x)^2}\right), \tag{4}$$

where x is the position from the start of the roll, r is the roll radius, λ is the neutron mean free path, x_e is the position of the roll peak, and $\Delta x = x_e - x$. The analytical transmission $R(x)$ for the experimental parameters (given in Sec. III) was also validated using an MCNP6 forward-model (similar to that shown in Fig. 3). The total transmission function $T(x)$ is then constructed as follows:

$$T(x) = \begin{cases} a_1 x + b_1, & x < x_e - h, \\ R(x) + R_0, & x_e - h < x < x_e, \\ a_2 x + b_2, & x > x_e, \end{cases} \tag{5}$$

where h is the roll height (the sagitta) given by $h = r - \frac{1}{2}\sqrt{4r^2 - L^2}$, and L is the length of the tungsten block. Note that R_0 is the offset of the lower step to make $T(x)$ continuous. Linear corrections have been added to the top and bottom of the step to account for long-range blur due to scattering. These corrections are described by the slope and vertical offset for the bottom (a_1, b_1) and the top (a_2, b_2) of the step.

For an image blur described by $F(x)$, the ESF fit function $H(x)$ is then given by the convolution,

$$H(x) = T(x) \circledast F(x). \tag{6}$$

As described in Sec. I, the total image blur is a convolution of blur from the source and from the imaging system; let these be represented by $g(x)$ and $k(x)$, respectively. The blur from the imaging system is expected to be small relative to that of the neutron source and is assumed to be approximately Gaussian. This blur component $k(x)$ can be experimentally measured by placing a rolled edge at the detector plane, such that the magnification is ~1 and the total image blur is dominated by the optical system (the derivation of this limit for Gaussian $g(x)$ and $k(x)$ can be found in Ref. 9). As such, only the source component $g(x)$ needs to be optimized in the fit once $k(x)$ has been measured.

If the source profile is Gaussian distributed, the blur kernel $g(x)$ would be described by

$$g(x) = A \cdot \exp\left(-\frac{(x - x_e)^2}{2\sigma^2}\right), \tag{7}$$

with amplitude A and standard deviation σ. The total fit function thus employs seven parameters for optimization $(a_1, b_1, x_e, a_2, b_2, A, \sigma)$. Bounds should be established for each of the fit parameters based on the experimental conditions to discard non-physical solutions and hasten convergence.

Different analytic functions can be used to approximate the neutron source distribution and, hence, the blur kernel $g(x)$.[8,9,16] Although the source is modeled as Gaussian for this analysis, comparisons with Lorentzian, Bennett, and super-Gaussian distributions will be presented to explore uncertainty due to source shape in Sec. V. The aforementioned distribution functions are illustrated in Fig. 4. Note that source shape (or distribution) will be used moving forward to describe the blur kernel fit to the ESF, but physically, it is only a planar projection of the full neutron distribution [see Eqs. (1) and (2)].

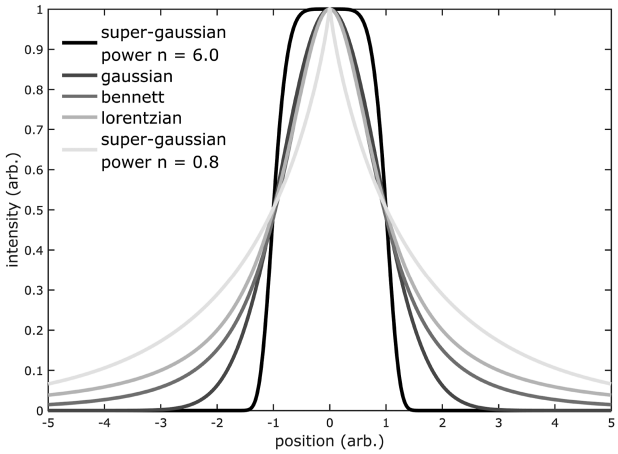

FIG. 4. Potential distribution functions for modeling the neutron source shape (blur kernel). Each has FWHM = 2 (arbitrary units).

The Lorentzian distribution has previously been used as an analytical approximation for the blur kernel of a finite neutron radiography source.[17] It can be described using

$$g(x) = \frac{A\gamma}{(x - x_e)^2 + \gamma^2}, \tag{8}$$

where the width fitting parameter has been modified to γ from σ in the Gaussian case to avoid overlap. The Bennett distribution has been used to model x-ray sources[8,9,18] and is given by

$$g(x) = A\alpha^2\left(\alpha^2 + (x - x_e)^2\right)^{-3/2}, \tag{9}$$

where the width parameter is α.

Theoretically, if the experimental conditions are constant and a sufficient number of the fit parameters are tightly constrained (if not known), the source shape could potentially be inferred using a generalizable distribution function for $g(x)$. One such function is the generalized normal distribution, or the super-Gaussian[19,20]

$$g(x) = A \cdot \exp\left(-\left|\frac{(x - x_e)}{\Sigma}\right|^n\right), \tag{10}$$

with the width parameter Σ to match the notation in Ref. 20. The power n in the exponential allows the distribution function itself to be optimized; hence, n would be an additional fit parameter. However, it is important to note that any long-range scattering terms (a_1, b_1, a_2, b_2) should be well-constrained to avoid overlap with the tails of the blur distribution.

The calculated spot size of the neutron source depends on the blur distribution as well as the definition for radiographic spot size, which varies in the literature (see Ref. 8 for discussion and comparison of the various metrics). For concision, the definition we will adopt in this study will be the full-width at half-max (FWHM) of the source distribution. The analytical FWHM of the aforementioned distribution functions is given in Table I.

These analytical methods were utilized in a combined fitting algorithm to infer the neutron spot size from experimental radiographs, where the measured ESF, tungsten edge dimensions, and magnification were the only required input parameters. The algorithm calculates the ideal (unblurred) edge response, $T(x)$, given in Eq. (5), using the input edge parameters to calculate $R(x)$ (the remaining variables, a_1, b_1, a_2, b_2, x_e, are constrained fit parameters). The ideal edge $T(x)$ is then convolved with an initial total blur kernel, $F(x)$, that is a convolution of the systematic blur $k(x)$ (measured when $M \sim 1$, modeled as Gaussian) and the initial-guess source blur $g(x)$, which has embedded fit parameters. Least-squares nonlinear regression is then used to optimize the fit parameters through iteration based on the Trust-Region-Reflective (TRR) algorithm.[21] The same results were obtained with the Levenberg–Marquardt algorithm,[22,23] but this routine was more sensitive (with regard to convergence) to starting values than TRR. The desired result, the neutron source FWHM, is inferred from the width fit parameter (σ, γ, α, or Σ) of the source blur $g(x)$. Note that for Gaussian $g(x)$, the optimization can also be performed with only the combined blur kernel $F(x)$ to get σ_{image}, and then the source vs detector components can be separated using Eq. (3).

TABLE I. FWHM values for relevant distribution functions. Variables σ, γ, α, and Σ are the width parameters of the distribution functions as described in Eqs. (7)–(10).

Gaussian	Lorentzian	Bennett	Super-Gaussian
$2\sigma\sqrt{2\ln(2)}$	2γ	$2\alpha\sqrt{2^{2/3}-1}$	$2\Sigma[\ln(2)]^n$

III. EXPERIMENTAL METHODS

The NNSS Sodium DPF was used as a neutron source to image tungsten test objects (note that the Sodium DPF has since been replaced by the ZEUS machine). At the time of this experiment, the DPF operated with a charging voltage of 30–50 kV for a peak current of 4 MA with a rise time of 6 μs.

The experimental setup is illustrated in Fig. 5. The DPF was located 0.85 m from a 1 m thick concrete collimator with a 20 cm diameter window where test objects were installed. Radiographs were taken of tungsten rolled edge apertures: 10 cm thick rectangular (denoted U1A 10 cm) and 10 cm thick L-shape (denoted L 10 cm), where thickness is defined along the line of sight of the neutron beam. The test object positions were varied slightly inside the collimator window: the U1A 10 cm edge was positioned 1.85 m from

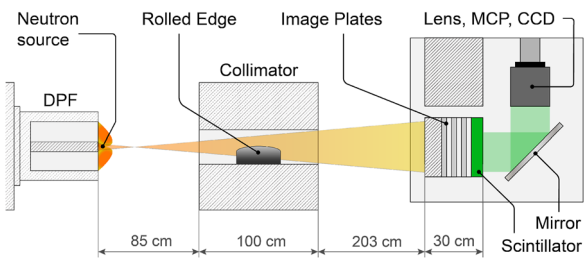

FIG. 5. Diagram of the experimental setup to image the DPF. The neutron source location was defined as the tip of the anode, though the pinch occurs in a region a few centimeters above.

the source, while the L 10 cm edge was positioned 1.75 m from the source. All edge rolls had a 1 m radius. Data were taken at slightly varying alignments (sequential 4 mm shifts normal to the rolled face) with the U1A 10 cm edge to probe alignment sensitivity. The L-shaped object was kept static and provided perpendicular edges to probe the ESF (and thus determine the neutron spot size) in two dimensions.

Neutrons were detected primarily using a scintillator-based imaging system, as shown in Fig. 5. A stack of 10 image plates interleaved with polyethylene was also positioned ~2 m from the collimating window for initial shots during camera timing adjustments and DPF pulse shaping, as well as for shots 8–9 (integrated). The scintillator-based imager consisted of a 4 cm thick EJ-204 plastic scintillator located 2.33 m from the collimator, coupled to a Photek S25 MCPII Image Intensifier and a Spectral Instruments SI-800 series CCD via a Spindler & Hoyer f/0.9 lens. Light from the scintillator was reflected to the lens using a flat mirror to prevent neutron irradiation of the optics.

In order to measure the detector blur, separate test objects (one 5 cm wide tungsten rolled edge, denoted NIS 5 cm, and one copper step wedge, 1 cm wide) were placed directly against the scintillator such that the image would have magnification $M \sim 1$. This was performed in order to measure the resolution of the optical system alone via the ESF of the rolled edge. Open-beam flat-field images were taken with no test objects in the aperture window, and dark-field images were taken by restricting light from entering the camera (lens cap). Rolled edge objects were then placed in the aperture window and imaged.

The camera gate was determined using the time-of-flight of the primary DT neutrons, which was calculated to be ~78 ns for the setup in Fig. 5. The MCP was triggered 10 ns before the primary neutron arrival time (55 ns after the expected gamma-ray arrival time) and gated on for a 60 ns window. In addition to gating, the scintillator was shielded by 1 inch of tungsten along the beam and was surrounded by tungsten and lead bricks to minimize scattering.

IV. RESULTS AND DISCUSSION

Images captured by the scintillator-based system were each corrected for thermal noise in the detector via dark-field subtraction and detector sensitivity via flat-field normalization; all images were first scaled by yield. The corrected images from four different configurations are shown in Fig. 6.

The ESF from each image was calculated by averaging over a rectangular region of interest (ROI) perpendicular to the rolled edge, an example of which is shown in Fig. 6(c). Note that the image was rotated such that a rectangular ROI would be perpendicular to the edge. ROI selection was based on collecting sufficiently large statistics parallel to the edge while keeping the location and size roughly constant between shots of the same rolled edge. The ROI of shots 3, 5, and 6 (the U1A edge) could not extend as far past the edge (into the full-intensity region of the image) as the other shots in order to avoid fitting to saturated data.

Image blur was determined using the fit routine described in Sec. II for a Gaussian neutron source distribution; discussion of alternate source profiles is presented in Sec. V. The resulting fits for Fig. 6(a) (detector blur) and Fig. 6(d) (detector and source blur of a vertical rolled edge) are shown in Figs. 7 and 8, respectively. Note that the Gaussian shown in Fig. 8 is for the source alone, having accounted for the detector blur found in Fig. 7. Fitting to the LSF was also attempted using Savitzky–Golay smoothing and numerical differentiation, but was found to produce significantly higher uncertainties in the calculated FWHM.

The average inherent blur in the optical system was found to be 2.36 ± 0.34 mm from the two calibration shots. Detector blur was likely dominated by the 4 cm thick monolithic plastic scintillator, as discussed previously.[10] Modeling this blur component as Gaussian

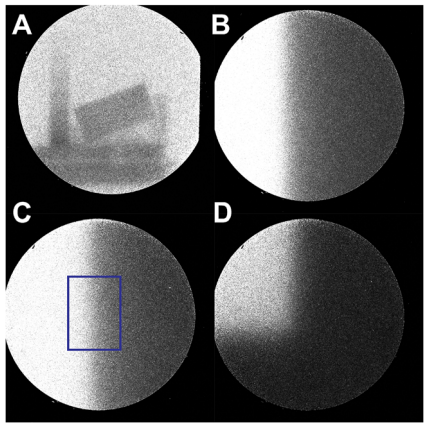

FIG. 6. Scintillator-based images of tungsten rolled edges in units of intensity. Image A shows the NIS 5 cm tungsten block and copper step wedge on an optical stage positioned against the scintillator for calibration (shot 2). For scale, the width of the NIS block in image A ($M \sim 1$) is 5 cm. Images B (shot 3) and C (shot 4) show the U1A 10 cm edge, where the edge in C was translated 4 mm right (with respect to the image) from B. Image C also shows an example region of interest (ROI) used for determining the ESF perpendicular to the vertical edge. Image D (shot 8) shows the L 10 cm edge that provides both a vertical and horizontal rolled edge.

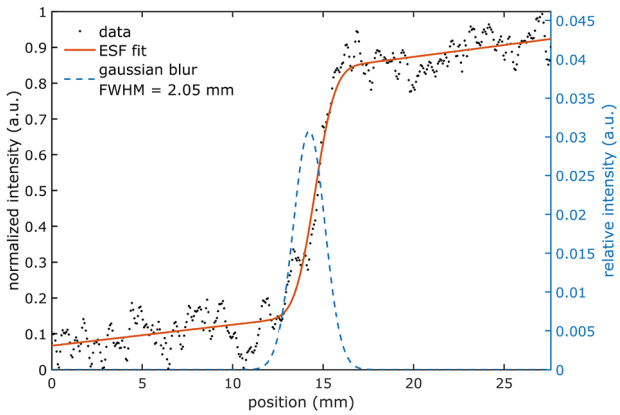

FIG. 7. Edge lineout with ESF fit and corresponding Gaussian source kernel for the detector blur—fit FWHM is 2.05 mm.

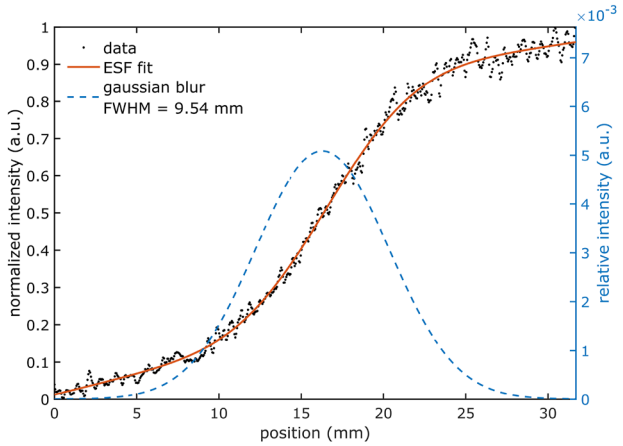

FIG. 8. Edge lineout with ESF fit and Gaussian source kernel for the vertical edge of the L object in shot 8—fit FWHM is 9.54 mm.

with FWHM = 2.36 ± 0.34 mm for $k(x)$ in the optimization routine, the source-specific blur $g(x)$ is then fit as described in Sec. II. The resulting FWHM values for a Gaussian neutron source are compiled in Table II.

The spot size uncertainties listed in Table II were determined by fitting the ESF at different locations along the edge and calculating the standard deviation of the fits. This metric captures the systematic uncertainties, which were found to dominate over statistical uncertainties from curve fitting. The statistical uncertainty was calculated by the optimization solver for the FWHM fitting parameter (σ, γ, α).

The dominant sources of systematic uncertainty are believed to be edge metrology, scattering, and alignment with the source, namely for the L-edge. As seen from Table II, the spot size uncertainties for fits to the L-edge are larger than those with the U1A edge. Another source of uncertainty is image saturation, which reduces the extent of the ESF that can be fit. This impacted shots 3, 5, and 6, which were saturated past the edge at the upper plateau and show a smaller spot size than the comparable shot with no saturation (shot 4). While these fits (shots 3, 5, and 6) capture enough of the edge to reasonably bind the ESF, data lost in the saturation region would be needed to better constrain the fits and reduce uncertainty.

Although the source size has been assumed to not vary significantly between shots, an estimate of the source size variability can theoretically be obtained by comparing shots 8 and 9, in which no experimental parameters were changed. This comparison yields <1 mm of variability, but with a small sample size and ~1 mm of uncertainty in measurement.

The average FWHM of the DPF source, averaging over the different edges and alignments, was determined to be 10.8 ± 1.2 mm along the horizontal direction and 8.6 ± 1.2 mm along the vertical direction, with respect to the image plane. The uncertainty of these values is taken to be the larger of either the standard deviation of the FWHM values or the propagated FWHM error

TABLE II. Experimental description and spot size results for neutron radiographs. Note that *M* is the image magnification and *RMSE* is the root-mean-square error of the ESF fit. Shots with 4 mm alignment shifts refer to the tungsten object being translated normal to the rolled face or in the $-y$ direction using the coordinate system shown in Fig. 3.

Shot	Rolled edge	M (D_2/D_1)	Neutron yield	Gaussian FWHM (mm)	FWHM error (mm)	ESF fit, *RMSE*
Calibration images (detector blur)						
1	NIS 5 cm	N/A	5.81×10^{11}	2.05	0.29	0.046
2	NIS 5 cm	N/A	7.40×10^{11}	2.67	0.39	0.043
Vertical aperture edge, 4 mm alignment shifts						
3	U1A 10 cm	1.20	1.89×10^{12}	7.75	0.85	0.014
4	U1A 10 cm	1.20	1.29×10^{12}	8.81	1.21	0.018
5	U1A 10 cm	1.20	1.32×10^{12}	7.92	0.85	0.021
6	U1A 10 cm	1.20	1.38×10^{12}	7.36	0.99	0.013
Vertical aperture edge						
8	L 10 cm	1.30	1.16×10^{12}	9.54	0.94	0.021
9	L 10 cm	1.30	1.12×10^{12}	10.32	1.31	0.024
Horizontal aperture edge						
8	L 10 cm	1.30	1.16×10^{12}	11.42	1.06	0.025
9	L 10 cm	1.30	1.12×10^{12}	10.19	2.12	0.027

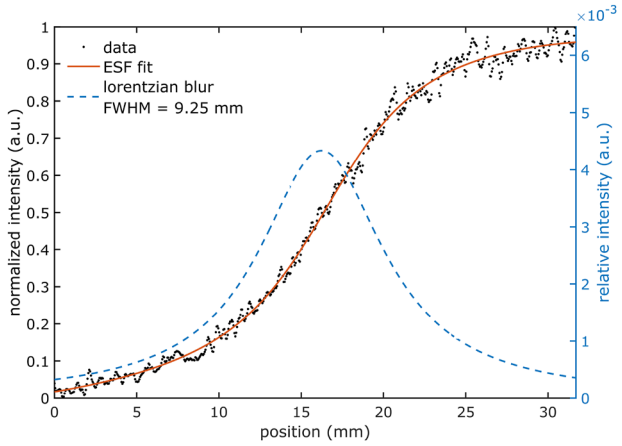

FIG. 9. ESF fit for a Lorentzian source and Gaussian detector blur for the vertical edge of shot 8. The fit spot size is 9.25 mm.

from all measurements in the average. These results are consistent with separate spot size measurements of the Sodium DT DPF using tungsten penumbral apertures rather than orthogonal rolled edges.[4]

V. DISCUSSION OF SOURCE SHAPE

As described in Sec. II, the image blur kernel should depend on the neutron source distribution. Although it was assumed Gaussian for the results in Table II, there are alternate analytical functions that can be used to fit the data. The systematic uncertainties in this experiment make it difficult to infer the source shape explicitly with any statistical certainty—that is, to back out the distribution using the super-Gaussian and/or other functions described in Sec. II. However, a comparison of different source distributions is presented in order to determine how significantly the source shape impacts the results for spot size.

Optimization with the generalized super-Gaussian profile revealed a consistent trend to power $n \leq 2$—that is, the fit routine consistently converged to a kernel equivalent to or sharper than a traditional Gaussian rather than a flat-top, which did not fit any of the data with comparable quality. Analytic $n < 2$ distributions include the Lorentzian and Bennett profiles described in Sec. II. Without information on source shape variation between shots, constant analytic functions (Gaussian, Lorentzian, and Bennett) were explored in place of the generalized super-Gaussian beyond this point.

An example of an ESF fit with a Lorentzian blur kernel for the same image as Fig. 8 is shown in Fig. 9. The total blur includes the Lorentzian source with the FWHM shown in Fig. 8, as well as the Gaussian blur of the imaging system (as described in Secs. I and II) with an average FWHM of 2.36 ± 0.34 mm (calculated in Sec. IV). Similar fitting was performed for all shots in Table II, the results of which are presented in Table III along with a goodness-of-fit metric, the root-mean-square-error (RMSE). The RMSE metric depends on the ROI size and is hence valid for comparison between fits for the same shot.

As seen from the comparable RMSE between fits for the same shot in Table III, the spot size measurement is dependent on the neutron source distribution. The most significant difference is found in shot 6 between the Lorentzian and Gaussian profiles of 1.6 mm, with the Lorentzian predicting a smaller effective spot. Future measurement of the DPF source shape and/or improved characterization of long-range scattering in this experiment could be used to determine which fits in Table III best describe the true neutron source.

TABLE III. Comparison of fit FWHM values using varied source distributions (Gaussian, Lorentzian, and Bennett). Consistent with Table II, shots with 4 mm alignment shifts refer to the tungsten object being translated normal to the rolled face, or in the $-y$ direction using the coordinate system in Fig. 3.

Shot	Gaussian FWHM (mm)	Gaussian *RMSE*	Lorentzian FWHM (mm)	Lorentzian *RMSE*	Bennett FWHM (mm)	Bennett *RMSE*
Vertical aperture edge, 4 mm alignment shifts						
3	7.75 ± 0.85	0.014	6.90 ± 0.96	0.015	7.20 ± 0.78	0.014
4	8.81 ± 1.21	0.018	8.68 ± 1.19	0.018	8.96 ± 0.98	0.018
5	7.92 ± 0.85	0.021	6.33 ± 1.02	0.023	6.92 ± 0.81	0.022
6	7.36 ± 0.99	0.013	5.76 ± 0.91	0.012	6.27 ± 0.82	0.012
Vertical aperture edge						
8	9.54 ± 0.94	0.021	9.25 ± 0.91	0.020	9.43 ± 0.89	0.020
9	10.32 ± 1.31	0.024	10.56 ± 1.34	0.024	10.28 ± 1.19	0.024
Horizontal aperture edge						
8	11.42 ± 1.06	0.025	10.88 ± 1.79	0.025	11.23 ± 1.64	0.025
9	10.19 ± 2.12	0.027	10.75 ± 1.70	0.027	10.35 ± 1.83	0.027

VI. COMPARISON TO SIMULATION

The plasma focus has been well-studied in the literature using 1D theory and scaling laws, as well as fluid, kinetic, and hybrid simulations.[6,24–28] The varied time scales and plasma conditions between successive phases in the DPF make it difficult to model with any one approach. For example, while a fluid description is generally adopted for the plasma run-down phase for computational efficiency, a kinetic description is required to predict beam-target neutron production resulting from the pinch.[25] The modeling presented in Ref. 6 explored the pinch dynamics of the DT DPF studied herein using high-fidelity 2D and 3D magnetohydrodynamic (MHD) simulations. Given the plasma conditions leading to and during the pinch formation, the MHD treatment is well justified. These MHD simulations are relatively high resolution, providing detailed information on the flow dynamics, including instabilities (see below). Modeling of the pinch formation, instabilities, and electric fields was conducted using the LA-COMPASS[29] numerical MHD solver, while the beam-target neutron production and energy spectrum were explored from the MHD solution using a custom kinetic model.

The MHD results show that the pinches formed have finite sizes, both in their radial and axial extent,[6] as shown in Fig. 10. In general, during the run-in phase leading to pinch formation, the interface between the plasma front and the magnetic field region undergoes the Kelvin–Helmholtz instability. This dynamic process breaks up the length of the cylindrical pinch and also causes density variations along the axial direction, which ultimately determines the axial size of the various pinches. Meanwhile, as the pinch forms, the central plasma pressure increases dramatically, impeding the magnetic pinch force and producing a radial extent over which the pinch can stagnate. This is depicted in both the 2D and 3D simulations, as shown in Fig. 10. In the 2D (r, z) simulation, one can see that a major pinch has formed at the height $z \sim 63 - 64$ cm with a radius $r \sim 4$ mm (a second, weaker pinch at height $z \sim 62$ cm is also forming). This means that the main pinch will have an axial extent of ~10 mm and a radial extent of ~4 mm. In 3D simulation, the pinch has 3D features deviating from cylindrical symmetry due to the kink instability. The regions with the highest density can be off-axis and no longer form a perfect cylinder, though the axisymmetric component is still dominant, as shown in Fig. 10. Both 2D and 3D simulation results show that the strongest pinches have a finite radial width, though 2D simulations have the inherent limitation of not capturing the asymmetric features around the axis. The axial extent of the highest density region is ~10 mm, and the radial extent is ~5 – 7 mm.

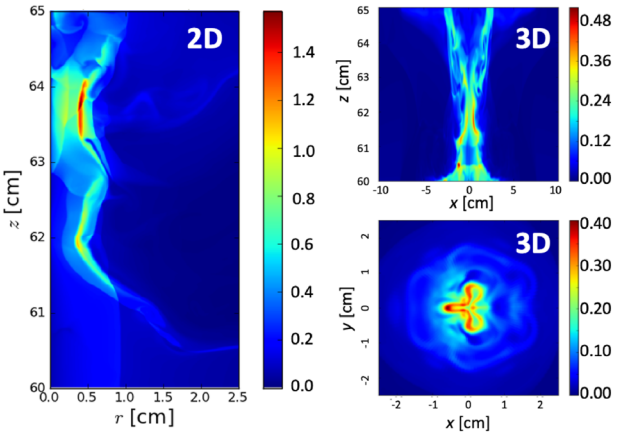

FIG. 10. MHD simulation of the DPF pinch formation showing the density (in units of 10^{20} cm^{-3}) at the time when the pinch density is highest. (left) 2D (r, z) simulation showing a major pinch at height $z \sim 63 - 64$ cm with a radius $r \sim 4$ mm. (right) 3D simulation showing a major pinch at height $z \sim 61 - 62$ cm with a transverse extent $r \sim 5 - 7$ mm (see Ref. 6 for details). Note that the horizontal/vertical directions referenced in Tables II and III correspond to orthogonal lineouts in the x, y planes of the end-on view (lower right).

Coupling these MHD results with the kinetic modeling, the neutron source is found to be pulsed in correlation with the high density pinches (shown in Fig. 10). This simulation result strongly indicates that the pinch that produces the strongest neutron pulse has a finite radial width. Although the radial extent of the high density pinches is consistent with the experimental measurements, the beam-target production from collisions with the dense plasma target during break-up will also impact the predicted spot size. A detailed comparison between the simulation results and experimental measurements (including the timing of pulses) is still being investigated and will be discussed in future publications.

The MHD simulations and kinetic modeling also predict that the DT neutron energy spectrum should be up-shifted due to beam-target interactions. The calculated spectrum is non-symmetric and peaked at 15 MeV. The experimental setup used to measure the spot size was gated to the expected arrival time of thermonuclear DT neutrons (14.1 MeV) from the anode tip in order to discriminate photons. Although it is unlikely that a significant fraction of the neutron signal was gated out due to this effect, future experiments could explore optimization of the timing window using co-timed neutron time-of-flight detectors.

VII. CONCLUSIONS AND OUTLOOK

The neutron spot size of the Sodium DT DPF was measured using the ESF from neutron radiographs of tungsten rolled edge test objects. The spot size was found to be 10.8 ± 1.2 mm FWHM horizontally and 8.6 ± 1.2 mm FWHM vertically, averaging over varied rolled edges and alignments with the source. Systematic uncertainties and source shape ambiguity introduced quantitative and qualitative uncertainty on the spot size, which could be reduced in future experiments with improved edge metrology, characterization/reduction of neutron scattering, and a larger sample size. Results are consistent with modeling performed using MHD, which suggests the neutron production volume is driven by pinches far from the axis, increasing the effective neutron spot size. Further study could also explore the neutron source distribution explicitly using a similar experimental configuration. Although a best-fit analytic function for the average neutron source shape cannot be concluded from these data, the comparable Lorentzian/Bennett fit results suggest that it could be more sharply peaked than the Gaussian assumption. The large spot size indicates that the DPF should be used to drive flash neutron radiography at low magnification, where spot size does not dominate spatial blur.

ACKNOWLEDGMENTS

The authors would like to acknowledge the DPF Head of Operations, Nathan Sipe, as well as his team operating the DPF at the Nevada National Security Site. The authors would also like to acknowledge Danielle Schaper for her assistance with article preparation. This work was performed for the National Nuclear Security Administration under the auspices of the U.S. Department of Energy by the Los Alamos National Laboratory under Contract No. 89233218CNA000001 and by the Nevada National Security Sites, managed and operated by Mission Support and Test Services, under Contract No. DE-NA0003624. The article preparation was supported in part by the National Science Foundation Graduate Research Fellowship under Grant No. DGE 1841052.

AUTHOR DECLARATIONS

Conflict of Interest

The authors have no conflicts to disclose.

Author Contributions

L. Tafoya: Formal analysis (lead); Investigation (supporting); Methodology (equal); Visualization (lead); Writing – original draft (lead); Writing – review & editing (equal). **V. Geppert-Kleinrath**: Formal analysis (lead); Investigation (lead); Methodology (equal); Writing – original draft (equal); Writing – review & editing (equal). **J. Allison**: Investigation (lead). **S. Baker**: Investigation (equal); Methodology (equal); Resources (equal). **J. Bundgaard**: Investigation (equal); Resources (equal). **M. Freeman**: Formal analysis (equal); Investigation (lead); Writing – review & editing (equal). **A. Hayes-Sterbenz**: Formal analysis (supporting); Software (equal). **G. Jungman**: Formal analysis (supporting); Software (equal). **H. Li**: Formal analysis (supporting); Software (equal); Writing – original draft (equal). **S. Li**: Formal analysis (supporting); Software (equal). **D. Lowe**: Investigation (equal); Resources (equal); Writing – original draft (supporting). **J. Tybo**: Investigation (lead). **C. Wilde**: Investigation (lead); Methodology (equal).

DATA AVAILABILITY

The data that support this study are available from the corresponding author upon reasonable request and security review.

REFERENCES

[1] F. E. Merrill, "Imaging with penetrating radiation for the study of small dynamic physical processes," Laser Part. Beams **33**, 425–431 (2015).
[2] N. King, E. Ables, K. Adams, K. Alrick, J. Amann, S. Balzar, P. Barnes, Jr., M. Crow, S. Cushing, J. Eddleman, T. Fife, P. Flores, D. Fujino, R. Gallegos, N. Gray, E. Hartouni, G. Hogan, V. Holmes, S. Jaramillo, J. Knudsson, R. London, R. Lopez, T. McDonald, J. McClelland, F. Merrill, K. Morley, C. Morris, F. Naivar, E. Parker, H. Park, P. Pazuchanics, C. Pillai, C. Riedel, J. Sarracino, F. Shelley, Jr., H. Stacy, B. Takala, R. Thompson, H. Tucker, G. Yates, H.-J. Ziock, and J. Zumbro, "An 800-MeV proton radiography facility for dynamic experiments," Nucl. Instrum. Methods Phys. Res., Sect. A **424**, 84–91 (1999).
[3] J. W. Mather, "Investigation of the high-energy acceleration mode in the coaxial gun," Phys. Fluids **7**(11), S28 (1964).
[4] M. S. Wallace, A. Neilsen, and E. C. Dutra, "High-fidelity dynamic neutron imaging and radiography for subcritical experiments and other applications (final report)," Technical Report, Nevada National Security Site (Report No DOE/NV/03624-1401) (2022).
[5] A. Schmidt, E. Anaya, M. Anderson, J. Angus, S. Chapman, C. Cooper, O. Drury, C. Goyon, S. Hawkins, D. P. Higginson, I. Holod, E. Koh, A. Link, D. Max, M. McMahon, J. Mitrani, Y. Podpaly, A. Povilus, and D. Van Lue, "First experiments and radiographs on the megajoule neutron imaging radiography (MJOLNIR) dense plasma focus," IEEE Trans. Plasma Sci. **49**, 3299–3306 (2021).
[6] H. Li, S. Li, G. Jungman, and A. Hayes-Sterbenz, "Dense plasma focus modeling," Technical Report LA-UR-17-25546, 2017.
[7] F. D. McDaniel, B. L. Freeman, and C. M. Fowler, "Applications of a neutron-producing dense plasma focus," in *International Conference Neutrons in Research and Industry*, edited by G. Vourvopoulos (International Society for Optics and Photonics, 1997), Vol. 2867, pp. 517–520.
[8] C. Ekdahl, "Characterizing flash-radiography source spots," J. Opt. Soc. Am. A **28**, 2501–2509 (2011).
[9] A. E. Schach von Wittenau, C. M. Logan, and R. D. Rikard, "Using a tungsten rollbar to characterize the source spot of a megavoltage bremsstrahlung linac," Med. Phys. **29**, 1797–1806 (2002).
[10] V. Geppert-Kleinrath, P. L. Volegov, C. A. Wilde, L. Tafoya, E. Mendoza, J. Vaughan, V. Fatherley, and C. Danly, "Lens design challenges for scintillator-based neutron imaging," in *Radiation Detectors in Medicine, Industry, and National Security XIX*, edited by G. P. Grim, L. R. Furenlid, H. B. Barber and J. A. Koch (International Society for Optics and Photonics, 2018), Vol. 10763, p. 107630P.
[11] V. Geppert-Kleinrath, M. S. Freeman, C. R. Hurlbut, F. Merrill, J. R. Tinsley, P. Volegov, and C. Wilde, "A liquid VI scintillator cell for fast-gated neutron imaging," Rev. Sci. Instrum. **89**, 10I142 (2018).
[12] D. N. Fittinghoff, N. Birge, and V. Geppert-Kleinrath, "Neutron imaging of inertial confinement fusion implosions," Rev. Sci. Instrum. **94**, 021101 (2023).
[13] C. J. Werner *et al.*, "MCNP6.2 Release Notes," Report LA-UR-18-20808, Los Alamos National Laboratory, 2018.
[14] K. Kohm, "Modulation transfer function measurement method and results for the orbview-3 high resolution imaging satellite," in *Proc XXXVB1* (International Society for Photogrammetry and Remote Sensing, 2004).
[15] G. F. Knoll, *Radiation Detection and Measurement*, 4th ed. (John Wiley & Sons Inc., 2010).
[16] C. Ekdahl, "Further metrics for flash-radiography source spots," arXiv:2112.05271 [physics.acc-ph] (2021).
[17] A. A. Harms, B. K. Garside, and P. S. W. Chan, "Edge-spread function in neutron radiography," J. Appl. Phys. **43**, 3863–3867 (1972).
[18] W. H. Bennett, "Magnetically self-focussing streams," Phys. Rev. **45**, 890–897 (1934).
[19] S. Nadarajah, "A generalized normal distribution," J. Appl. Stat. **32**, 685–694 (2005).
[20] S. Beirle, J. Lampel, C. Lerot, H. Sihler, and T. Wagner, "Parameterizing the instrumental spectral response function and its changes by a super-Gaussian and its derivatives," Atmos. Meas. Tech. **10**, 581–598 (2017).
[21] J. J. Moré and D. C. Sorensen, "Computing a Trust region step," SIAM J. Sci. Stat. Comput. **4**, 553–572 (1983).
[22] K. Levenberg, "A method for the solution of certain non-linear problems in least squares," Q. Appl. Math. **2**, 164–168 (1944).
[23] D. Marquardt, "An algorithm for least-squares estimation of nonlinear parameters," J. Soc. Ind. Appl. Math. **11**, 431–441 (1963).
[24] D. T. Offermann, D. R. Welch, D. V. Rose, C. Thoma, R. E. Clark, C. B. Mostrom, A. E. W. Schmidt, and A. J. Link, "Transition from beam-target to thermonuclear fusion in high-current deuterium *z*-pinch simulations," Phys. Rev. Lett. **116**, 195001 (2016).
[25] N. Bennett, M. Blasco, K. Breeding, D. Constantino, A. DeYoung, V. DiPuccio, J. Friedman, B. Gall, S. Gardner, J. Gatling, E. C. Hagen, A. Luttman, B. T. Meehan, M. Misch, S. Molnar, G. Morgan, R. O'Brien, L. Robbins, R. Rundberg, N. Sipe, D. R. Welch, and V. Yuan, "Development of the dense plasma focus for short-pulse applications," Phys. Plasmas **24**, 012702 (2017).

[26]D. R. Welch, D. V. Rose, C. Thoma, R. E. Clark, C. B. Mostrom, W. A. Stygar, and R. J. Leeper, "Kinetic simulation of thermonuclear-neutron production by a 10^7- A deuterium Z pinch," Phys. Plasmas **17**, 072702 (2010).
[27]A. Schmidt, V. Tang, and D. Welch, "Fully kinetic simulations of dense plasma focus *z*-pinch devices," Phys. Rev. Lett. **109**, 205003 (2012).
[28]J. R. Angus, A. J. Link, and A. E. W. Schmidt, "One-dimensional theory and simulations of the dynamic Z-pinch," Phys. Plasmas **27**, 012108 (2020).
[29]S. Li and H. Li, "A fast parallel simulation code for interaction between proto-planetary disk and embedded proto-planets," Technical Report, LA-UR-09-2968, 2009.